

Article

Customised Microporous Carbon 3D Structures with Good Mechanical Properties and High Nitrogen Content Obtained from Whey Powders

Raúl Llamas-Unzueta ¹, Luis A. Ramírez-Montoya ^{1,2,*}, J. Angel Menéndez ¹
and Miguel A. Montes-Morán ¹

¹ Instituto de Ciencia y Tecnología del Carbono, INCAR-CSIC, c/Francisco Pintado Fe 26, 33011 Oviedo, Spain; r.llamas@incar.csic.es (R.L.-U.); angelmd@incar.csic.es (J.A.M.); miguel.montes@csic.es (M.A.M.-M.)

² Laboratory for Research on Advanced Processes for Water Treatment, Engineering Institute, Universidad Nacional Autónoma de México (UNAM), Campus Juriquilla, Blvd. Juriquilla 3001, Juriquilla 76230, Querétaro, Mexico

* Correspondence: lramirez@ingen.unam.mx

Abstract: Novel customised carbon monoliths with a high specific surface area were synthesised by carbonisation plus activation of dehydrated whey powders, a biomass byproduct of the dairy industry. The whey powders were casted directly by pouring them into a desired mould. After a pseudo-sintering process promoted by the self-reaction of the whey components (mostly lactose and whey proteins) at moderate temperatures (ca. 250 °C), 3D porous carbons were obtained. The process did not require any binder or external overpressure to prepare the 3D porous carbons. Upon thermal activation with CO₂ or chemical activation with H₃PO₄ and KOH, the shape of the monolithic structure was preserved after the development of a microporous network (S_{BET} up to 2400 m²/g). Both thermal and chemical activation had little effect on the macroporosity of the monoliths. Activation of these 3D carbons had to be performed with care to avoid heterogeneous skin/core activation and/or overactivation. Highly porous monoliths (S_{BET} of 980 m²/g; open porosity of 70%) with outstanding compressive strength (10 MPa) could be obtained by thermal activation (CO₂) of whey monoliths at 850 °C for 1.5 h. Additionally, the use of whey as a precursor provided the carbon monolith with a relatively high nitrogen content (ca. 3 wt.%).

Keywords: porous carbon monolith; activation; whey; biomass carbon; mechanical properties



Citation: Llamas-Unzueta, R.; Ramírez-Montoya, L.A.; Menéndez, J.A.; Montes-Morán, M.A. Customised Microporous Carbon 3D Structures with Good Mechanical Properties and High Nitrogen Content Obtained from Whey Powders. *C* **2023**, *9*, 100. <https://doi.org/10.3390/c9040100>

Academic Editor: Jandro L. Abot

Received: 29 August 2023

Revised: 27 September 2023

Accepted: 17 October 2023

Published: 24 October 2023



Copyright: © 2023 by the authors. Licensee MDPI, Basel, Switzerland. This article is an open access article distributed under the terms and conditions of the Creative Commons Attribution (CC BY) license (<https://creativecommons.org/licenses/by/4.0/>).

1. Introduction

The manufacture of most carbon materials that are technologically relevant has strongly relied on the fossil fuel industry. The predicted gradual phase-out of this industry is thus expected to have a massive impact on the way technological carbons are made today, with carbon materials corporations being compelled to search for low-carbon alternatives, including precursors. In this scenario, biomass is expected to play a primary role as a precursor in several carbon markets in which its presence has been so far residual or non-existent [1–3].

Biomass is already a significant contributor to the industrial production of porous carbon materials. Activated carbon companies nowadays consume lignocellulosic biomass (wood and coconut shell mainly) to obtain porous carbon powders or granules, which are daily used products in a wide variety of activities including environmental and energy storage applications [4–6]. However, in a number of processes, 3D structured porous carbons (carbon monoliths) offer several advantages over powdered or granular ones [7–9]. Monolithic structures incorporate transport pores to reduce the pressure drop in continuous operations such as industrial filters [10,11]. They are also very relevant materials for heterogeneous catalytic reactors at the industrial level [12,13], and gas storage applications [14–16]. In all these applications, not only the porosity of the carbon material is

of paramount importance but also how the 3D carbon structure endures the operating conditions in industrial plants. In other words, 3D structured porous carbons should also have good mechanical properties, which makes the current fossil fuel-derived resins and binders (i.e., pitch) imperative in the manufacture of carbon monoliths [17–19].

There have been significant efforts to cut off ties with this undesirable dependence. Carboxymethyl cellulose (CMC) has been used as a green binder with remarkable results in terms of the mechanical properties of the resulting activated carbon monoliths [20]. However, the use of binders to agglomerate activated carbon powders has traditionally important drawbacks related to pore clogging [21,22]. Strategies based on binder-free monoliths from biomass precursors are scarce. Indeed, a very interesting methodology comprises the formation of slurries from activating agents such as H_3PO_4 or ZnCl_2 and lignocellulosic precursors [23–25]. These slurries are prone to be either uniaxially compressed or extruded to obtain monoliths that withstand carbonisation and washing of the activation by-products. On the other hand, sustainable approaches to a greener synthesis of 3D structured porous carbons comprise studies with a number of novel biomass-derived precursors including polysaccharides [26], tannins [27], or novel biomass wastes (i.e., beyond lignocellulosic precursors) [28]. Hydrothermal carbonisation (HTC) and other approaches also looked forward to obtaining 3D structured porous carbons, mainly carbon aerogels [29,30]. However, results in terms of the mechanical integrity of those green carbon monoliths have been, in general, rather limited.

We have recently discovered the possibility of obtaining 3D porous carbons with outstanding mechanical properties by direct carbonisation of whey powders poured on moulds [31]. Whey powders result after the spray-drying of liquid whey, a byproduct of cheese and casein production found in massive quantities in the dairy industry [32]. The relatively high organic matter (mainly lactose) load of liquid whey makes whey management a serious burden. Big dairy companies have invested important resources to valorise whey and an estimated 50% of liquid whey ends nowadays in food and feed industries [33,34]. Still, ca. 100 million tons of liquid whey are wasted each year worldwide [35]. Since, as detailed in [31], the mechanical properties of the 3D whey derived carbons compete with those prepared from conventional resins, whey should be then considered a robust biomass precursor to manufacture green carbon monoliths that can be used, for example, as bone scaffolds [36].

The porosity of the 3D whey-derived carbons have been also characterised in previous studies. The carbonisation of whey powders renders materials that are mainly macroporous, with limited meso- and micropore development, as determined by N_2 adsorption at cryogenic temperatures [31]. The aim of this work is to study the activation of whey carbon monoliths to improve their micro- and mesoporosity, which is compulsory for their use as adsorbents or catalysts/catalyst supports. Although KOH activation of whey powders has been reported before [37], as it has been that of non-fat powdered milk, a precursor similar to whey [38], the final product of these studies are activated carbon powders, which is not the purpose of this work.

2. Materials and Methods

2.1. Synthesis and Activation of the Whey-Derived Carbon Monoliths

The preparation of the custom-made microporous carbon 3D structures from whey comprises two steps: (i) pre-conformation of the 3D structure; (ii) carbonisation and/or activation.

For the pre-conformation of the 3D structures, whey powder (W) (CAPSA-Food, Granda, Spain) was poured into a 12 mm inner diameter glass tube. Details of W including its chemical composition have been reported elsewhere [31]. The pre-conformation step was carried out at 150 °C for 1 h in a lab stove. After this step, the W powder transformed into a solid rod of 12 mm diameter. The rod was then cut in cylinders of 30 mm height using a circular saw.

The cylinders were further carbonised at different temperatures in a tubular furnace (Carbolite, Hope Valley, UK) under N_2 (100 mL/min) with a heating rate and dwell time

of 10 °C/min and 1.5 h, respectively. The carbonised samples were labelled as CW_X, with X being the carbonisation temperature. Some of the carbonised whey cylinders were demineralised (samples CW_X_D) by acid (HCl) plus water washing in an ultrasonic bath.

Thermally activated samples (TAW) were first heat treated at up to 850 °C for 1.5 h under 100 mL/min N₂. After carbonisation, the temperature of the oven was set to the activation temperature (800–850 °C), the N₂ flux was switched to 50 mL/min CO₂ and kept at that activation temperature for 1–3 h. Finally, the monolith was cooled down in N₂ (100 mL/min). The TAW_X_Y samples' labelling code includes the activation temperature (X) followed by the dwelling time (Y).

Chemically activated samples (CASs) were prepared using both KOH and H₃PO₄ as activating agents (CH). KOH powder, H₃PO₄ (85% in water) and fuming HCl were purchased from Sigma-Aldrich (Schnelldorf, Germany). Milli-Q water was used for washing and impregnation procedures. The direct chemical activation of the pre-conformed monoliths was not feasible and a thermal stabilisation step was required prior activation. In the case of H₃PO₄ activation, the pre-conformed cylinders were heated up to 250 °C in the tubular furnace under N₂ (100 mL/min) for 1.5 h, whereas for KOH activation, the stabilisation temperature was set at 450 °C. The thermally stabilised monoliths (S) were then impregnated with different proportions of either KOH or H₃PO₄. This impregnation step was carried out by sonicating the monolith in 100 mL of a water solution of the CH at 80 °C for 2 h and then dried at 100 °C. It is important to mention that the integrity of the monolith remained unaltered after this stage. Afterwards, the impregnated monolith was placed in an alumina crucible and thermally treated at different temperatures for 1.5 h with a heating ramp of 10 °C/min under N₂ atmosphere (100 mL/min). After cooling down in N₂, the CAS samples obtained using KOH were washed with 1 M HCl under US during three cycles of 15 min each followed by vacuum filtration for each batch. Then, samples were washed with distilled water in an ultrasonic bath and filtrated. This procedure was performed for three consecutive 15 min washing cycles. The samples were finally dried at 110 °C in a convection oven overnight. For phosphoric activated samples, five washing cycles were performed using only sonicated water. The resulting monoliths were labelled as CAS_X_CH_Z, X being the heat treatment temperature, CH the activating agent (K for KOH and P for H₃PO₄) and Z the S:CH impregnation ratio.

2.2. Characterisation Methods

The thermogravimetric (TG) analyses of the W powders were carried out in a TGA Q5000 device from TA Instruments (New Castle, DE, USA) under N₂ and CO₂ atmospheres (20 mL/min) using a heating rate of 10 °C/min from room temperature to 1000 °C with sample masses of ca. 20 mg. For ash and moisture contents of the carbonised and activated monoliths (also ca. 20 mg), TGs were obtained using 20 mL/min of N₂ up to 900 °C and then switching to air (20 mL/min) for 30 min at that temperature. The moisture contents were calculated from the loss of weight at 110 °C. The ash content was estimated by the difference of the total loss of weight of the sample after combustion at 900 °C on air. The elemental analysis of the carbon monoliths was carried out in LECO (Geleen, The Netherlands) apparatuses (LECO CHNS-932, and LECO VTF-900 for oxygen content determination). The point of zero charge of the monoliths (pH_{PZC}) was determined by mass titration [39].

Nitrogen adsorption–desorption isotherms at −196 °C were performed in a Micromeritics Tristar II volumetric adsorption system, after outgassing the samples at 120 °C overnight. The specific surface area (S_{BET}) and micropore volume (V_{micro}) were calculated using the Brunauer–Emmett–Teller (BET) and Dubinin–Radushkevich (DR) models, respectively, while the pore size distributions (PSD) were calculated using the Density Functional Theory (DFT) model. The helium densities (ρ_{He}) were determined in an AccuPyc 1330 pycnometer (Micromeritics, Norcross, GA, USA). For the Hg intrusion technique, an AutoPore IV porosimeter (Micromeritics, GA, USA) was used. The Hg densities (ρ_{Hg}) and corresponding PSDs were determined from the Hg intrusion data up to a maximum

operating pressure of 227 MPa. For both He and Hg densities determination, samples were outgassed at 120 °C overnight.

Compressive strengths (S_u) were evaluated in an Instron Model 8562 (Instron, Norwood, MA, USA) device with a cell load of 10 kN and a test velocity of 0.5 mm/min. The final dimensions of the tested specimens were 12.25 ± 0.2 mm diameter and 22.5 ± 0.2 mm height. The compressive strength value is the maximum stress (load/area) that the specimen stood during the test. The elastic compressive moduli (E) were obtained from the slope of the linear elastic region of the stress vs. strain curve. For a given sample, the S_u and E values reported are the average of three compressive tests.

3. Results and Discussion

3.1. Customised 3D Structures Made of Carbonised Whey Powders

As shown in Figure 1, 3D monolithic porous carbons with different shapes and sizes were obtained by the simple carbonisation of pre-conformed W powders, depending on the selected mould (cubes, cylinders, spheres, hexagons, etc.). Even more sophisticated geometries, such as nuts or hollow cylinders, are possible. Also, the mechanical stability of the whey-derived carbon monoliths bears machining processes to obtain customised materials for a variety of applications. As pointed out in previous works [31], whey particles stick to each other by the self-reaction between the precursor constituents (lactose and whey proteins) during the heat treatment. Whey particles do not melt with temperature and both the pre-conformation and carbonisation/activation of the 3D structures is carried out in absence of any external template, binders or pressure. It should be finally mentioned that quantities of inorganic matter (6–13% ash contents, depending on the W batch and/or brand) remain in the carbon monoliths, mainly composed of Ca, K, Na, and P [31,40].

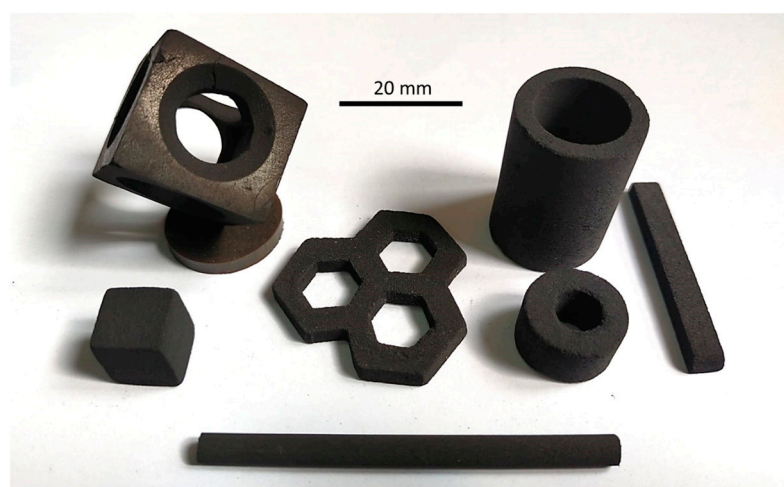


Figure 1. Examples of customised whey-derived carbon 3D structures made by simple moulding, or by moulding + machining.

3.2. Thermal Activation of the Whey-Derived 3D Carbons

As mentioned in the Introduction, whey carbon monoliths are essentially macroporous materials (maximum of the Hg intrusion PSD centred at 20–40 μm , see Section 3.4) and show no significant micro or mesoporosity, as measured by N_2 adsorption at -196 °C (Figure 2a). However, the adsorption of CO_2 at 0 °C on the same materials (Figure 2b) is significant and reveals the ultra-microporosity (pore sizes below 0.7 nm) of these materials. The ultra-microporosity is incipient in the low-temperature carbonised monoliths CW_450 and increases substantially as the carbonisation temperature rises up to 750 and 850 °C. Finally, higher carbonisation temperatures (CW_1000) result in a decrease in the volume of CO_2 adsorbed, thus suggesting the collapse of the narrow micropores. The relevant CO_2 adsorption on these materials, especially CW_750 and CW_850, opens the possibility of

transforming the whey-derived carbon 3D structures into activated carbon monoliths by thermal activation.

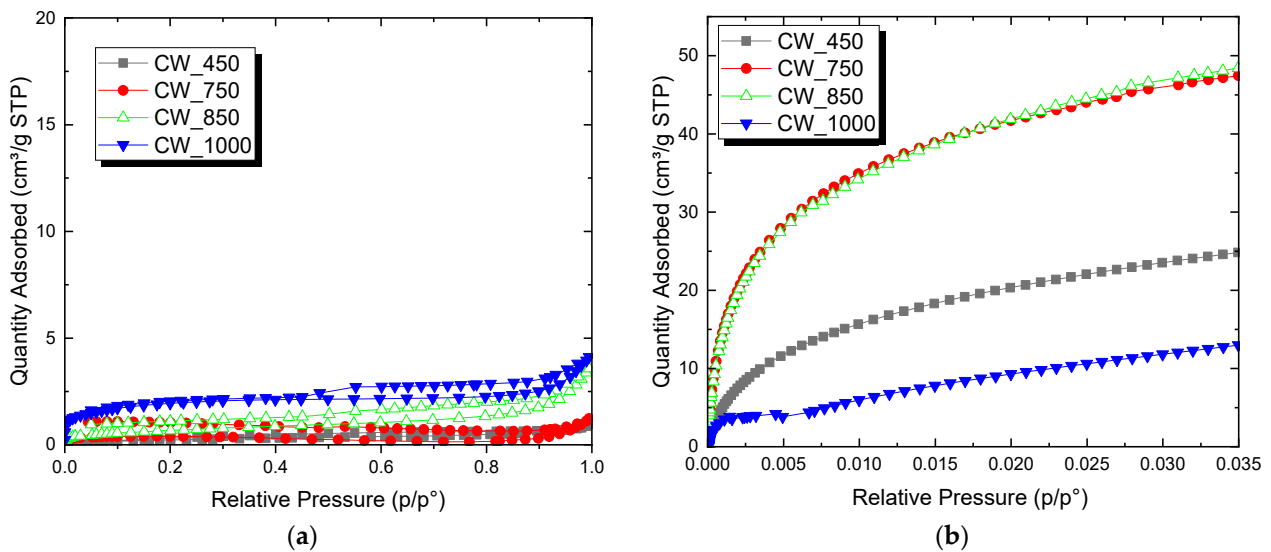


Figure 2. (a) N₂ adsorption isotherms (−196 °C); and (b) CO₂ adsorption isotherms (0 °C) on whey monoliths carbonised at different temperatures.

This was further confirmed by the TG analysis of the precursor W. Figure 3 shows the TG and DTG profiles of W heated in both N₂ and CO₂ atmospheres. Discussing first the TG profile of whey carbonisation, the TG curve is characterised by five stages. The first stage with the DTG peak at ca. 80 °C is attributed to the evaporation of the moisture remaining in the W sample. The second stage (130–160 °C) corresponds to the loss of crystalline water present in the α -lactose monohydrate (spray dried whey particles are a matrix of amorphous lactose in which lactose monohydrate crystals, proteins, fats and minerals are embedded). The reactions occurring in this temperature range are critical for the formation of 3D structures from W that withstand carbonisation. The release of crystalline water in this second stage is expected to boost the formation of melanoidins through the Maillard reactions between the lactose and the proteins in W. The successive thermal events (from 160 °C onwards) are thus complex and comprise the thermal evolution of unreacted lactose and whey proteins, on one side [31], and melanoidins, on the other [41,42].

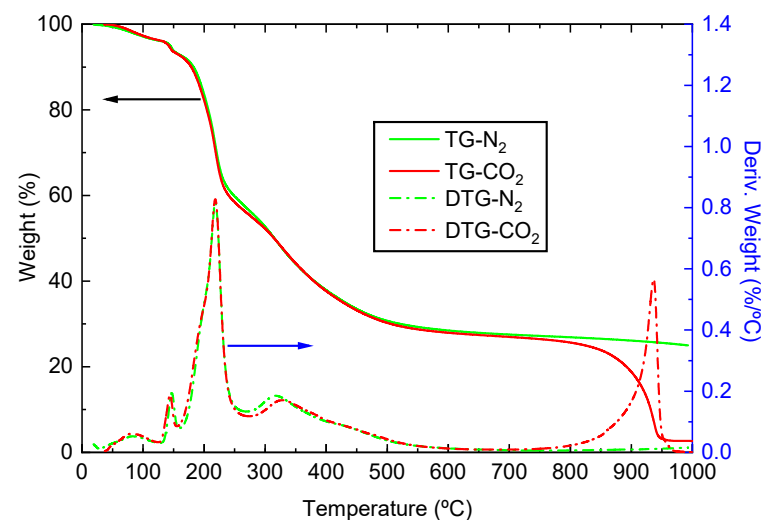


Figure 3. TG and DTG of the whey powders under N₂ and CO₂ atmospheres.

The TG of W in CO₂ is, as expected, virtually identical to that in N₂ during most of the temperature scan. Gasification starts at 720 °C, and the quick mass drop, also reflected in the sharpness of the corresponding CO₂ DTG band with maximum at 935 °C, indicates the relatively high reactivity of the W char when compared, for example, to conventional biomass chars such as coconut char [43]. This high reactivity of the whey char is a consequence of two contributions: (i) the high ultra-micropore volume of the CWs obtained at carbonisation temperatures above 700 °C (Figure 2b); and (ii) the existence of mineral matter catalysing the gasification. Analysis of the TG/DTG CO₂ profile of W suggests that the best temperature range for thermal activation of W chars is 800–850 °C, temperatures at which the gasification would be kept under (relative) control.

The activation of the W chars (CW_850) was thus carried out at 800 °C and 850 °C. Before showing and discussing the results obtained, a fundamental comment regarding the thermal activation of these monoliths should be pointed out. The thermal activation of the stocky 3D structures of carbonised whey in the tubular oven was quite tricky. Considering that, even when working with powders, the standard procedures of CO₂ activation recommend the deposit of thin layers over the crucible in order to facilitate the contact between the gas and the carbon material, the activation of a monolith represents a challenge. The CO₂ needs to diffuse into the whole cylinder in order to obtain a homogeneous activation, i.e., to minimise the differences of activation between the skin and the core of the monolith [44]. N₂ isotherms (−196 °C) of the monolith skin and core were thus measured by removing the outermost (approx. 1 mm) crust of the cylinders after activation. Although we were confident that the open macroporosity of the whey-derived chars would ease the diffusion of the CO₂ inside the cylinders, the initial experiments failed to provide homogeneous activation of the pieces. Regardless of the changes in the composition (relative proportion of CO₂ and N₂) and flux of the inlet gas, those initial experiments brought about either non-activated monoliths or only skin-activated monoliths. It was necessary to plug a substantial amount of quartz wool at the tube inlet (approx. 10 cm length), that helped to spread the laminar flow of CO₂, to succeed with differences between the skin and core being less than 10%. The results shown in Figure 4 and Table 1 correspond to the measurements of the whole (skin + core) monolith.

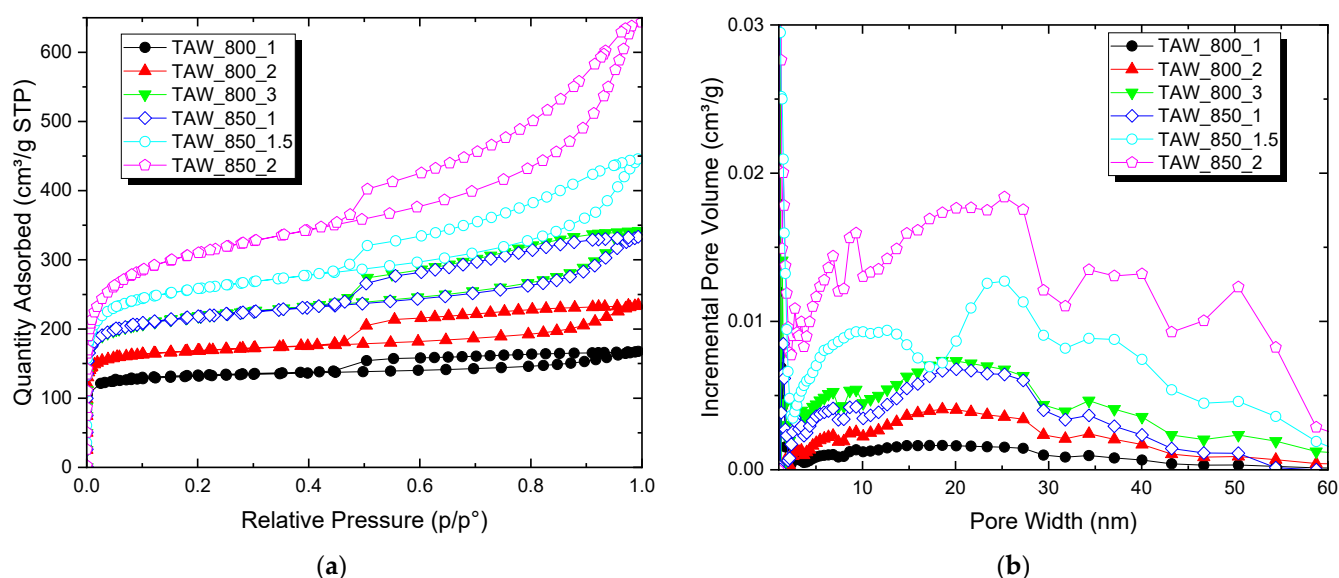


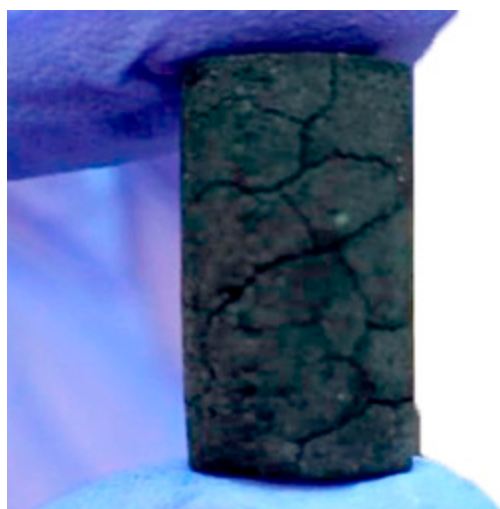
Figure 4. (a) N₂ adsorption isotherms (−196 °C); and (b) DFT pore size distributions of the thermally (CO₂) activated monoliths derived from whey.

Table 1. Selected textural parameters and yields of the thermally activated carbon monoliths.

Sample	S_{BET} (m^2/g)	$V_{\text{total}}^{\text{a}}$ (cm^3/g)	$V_{\text{micro}}^{\text{b}}$ (cm^3/g)	$V_{\text{meso}}^{\text{c}}$ (cm^3/g)	ρ_{He} (g/cm^3)	Yield ^d (%)	Burn-Off ^e (%)
CW_850	<10	0.001	-	-	2.00	22.4	0
TAW_800_1	500	0.287	0.205	0.082	2.07	17.2	23.2
TAW_800_2	663	0.363	0.261	0.102	2.00	15.0	33.0
TAW_800_3	834	0.529	0.332	0.197	1.98	12.3	45.1
TAW_850_1	839	0.516	0.331	0.185	2.01	12.3	45.1
TAW_850_1.5	981	0.689	0.377	0.312	2.01	10.1	54.9
TAW_850_2	1140	0.995	0.442	0.553	1.99	7.1	68.3

^a Calculated at $p/p^0 = 0.99$; ^b calculated with the DR method; ^c $V_{\text{meso}} = V_{\text{total}} - V_{\text{micro}}$; ^d expressed as $(\text{mass}_{\text{monolith}}/\text{mass}_{\text{whey}}) \times 100$; ^e expressed as $100 - [(\text{yield}_{\text{CW}_850}/\text{yield}_{\text{monolith}}) \times 100]$.

Thermal activation is effective at both temperatures, rendering materials that combine micro and mesoporosity (isotherm Type IV, Figure 4a). The monoliths activated at 800 °C show a limited development of the microporosity, with S_{BET} maximum values of 840 m^2/g after 3 h of dwell time. This very same value is obtained after only 1 h of CO_2 activation at 850 °C, whereas 2 h activation at this higher temperature brings about materials with S_{BET} values well above 1100 m^2/g . Due to the high reactivity of the whey-derived carbon, this relatively high surface area is attained at the expense of a high burn-off (68.3%, Table 1) of the whey char, which strongly limits the mechanical integrity of the resulting 3D structure (Figure 5). Profusion of cracks in the whey monoliths makes the activation conditions (2 h at 850 °C) unfeasible for their practical use, thus establishing the temperature and dwell time boundaries for thermal activation of these 3D structures with CO_2 . On the other hand, looking at the textural parameters of the activated monoliths at 850 °C (Table 1), there is a considerable gap between the specific surface area of the TAW_850_1 and TAW_850_2. We decided then to perform an additional activation experiment with a 1.5 h dwell time (sample TAW_850_1.5); the results are also included in Figure 4 and Table 1. The TAW_850_1.5 monoliths were free of external crevices.

**Figure 5.** An example of a monolith with crevices due to overactivation. This picture corresponds to TAW_850_2, but it is also representative of the chemically activated monoliths.

The gasification of the whey monoliths under the tested conditions encompasses not only the formation of micropores but also an enhancement of the mesoporosity. The pore size distribution in the mesopore range of these materials is very similar for all materials except TAW_850_1.5 (Figure 4b). They are wide distributions in which several maxima can be spotted at ca. 20, 35, and 50 nm. In the case of the TAW_850_1.5 mesopore size distribution, the maximum at 20 nm seems to further split into two bands at 10–12 nm

and 25 nm. The evolution of the micropore and mesopore volumes (Table 1) as the activation conditions become harsher confirms that a 850 °C and 2 h dwell is a point of inflection with $V_{\text{meso}} > V_{\text{micro}}$, thus suggesting that gasification of the char is widening the micropore network.

Figure 6 shows the relation between the burn-off and the specific surface area and micropore volume of the thermally activated samples. A good linear correlation exists in both cases.

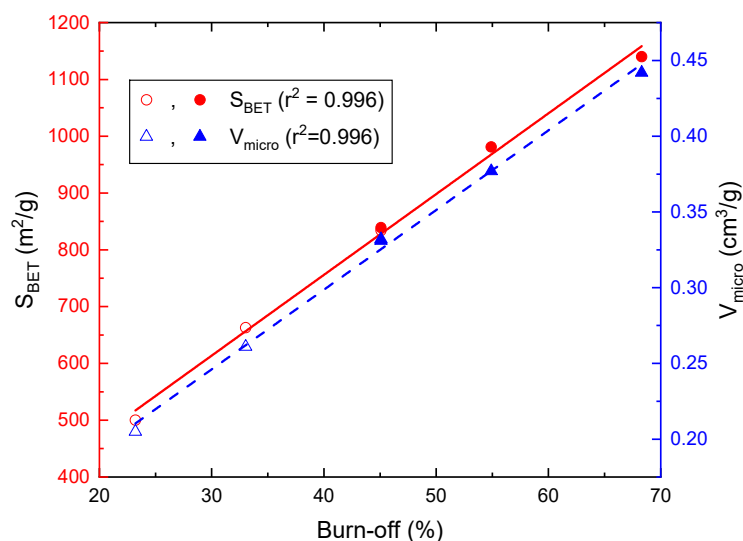


Figure 6. Specific surface area (S_{BET}) and micropore volume (V_{micro}) as a function of the thermal activation burn-off of the whey-derived activated carbon monoliths. Void and solid symbols correspond to the TAW_800 and TAW_850 monoliths, respectively.

3.3. Chemical Activation of the Whey-Derived 3D Structures

KOH and H_3PO_4 were selected as activating agents (CH) due to their well-known capacity to generate a microporous network into the carbon matrix. As detailed in the Section 2, the chemical activation was carried out over thermally stabilised monoliths. The direct activation of the whey brought about melted structures that did not keep the shape of the mould containing them, obtaining either powders (KOH activation) or foamy structures (H_3PO_4 activation). On the other hand, the issue that was pointed out when discussing the results of the thermal activation, regarding the homogeneity of the activated materials, was much less critical in the case of the chemical activation of the thermally stabilised monoliths. The macroporosity already present in these stabilised monoliths was well interconnected and the CH impregnation step was effective in reaching the inner parts of the stabilised monoliths. In addition, in the case of KOH it is also expected that the melting of the salt at temperatures above 360 °C will help the infiltration of CH into the monoliths and thus lead to a more homogeneous activation.

3.3.1. KOH Activation

Figure 7 shows the N_2 adsorption isotherms (−196 °C) of the KOH-activated samples and Table 2 summarises the principal textural parameters calculated from those isotherms. All N_2 isotherms are Type I with well-defined plateaus corresponding to highly microporous materials with slit-shaped pores in the micropore range, with the exception of CAS_750_K_1:1, which is a mixed Type I and IV isotherm with a hysteresis loop denoting the presence of mesopores ($V_{\text{meso}} = 0.137 \text{ cm}^3/\text{g}$, Table 2).

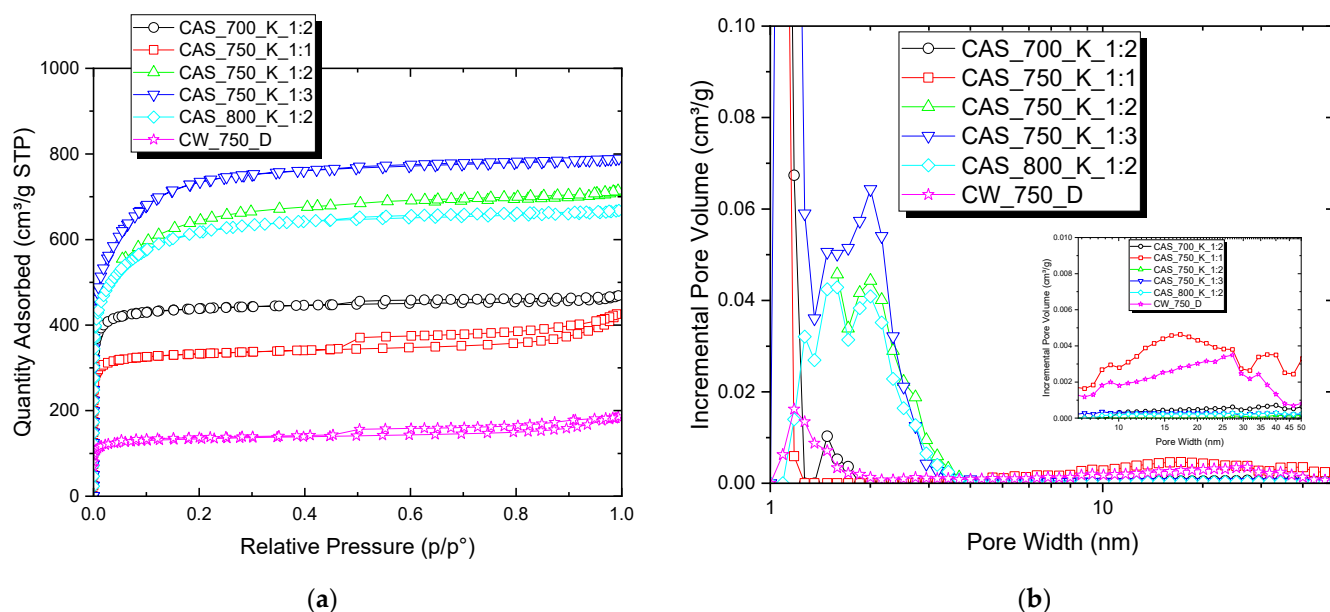


Figure 7. (a) N₂ adsorption isotherms (−196 °C); and (b) DFT pore size distributions of the chemically (KOH) activated monoliths derived from whey. Inset of (b) is a zoom of a selected area (5–50 nm).

Table 2. Selected textural parameters and yields of the chemically (KOH) activated carbon monoliths.

Sample	S _{BET} (m ² /g)	V _{total} ^a (cm ³ /g)	V _{micro} ^b (cm ³ /g)	V _{meso} ^c (cm ³ /g)	ρ _{He} (g/cm ³)	Yield ^d (%)
CW_750	<10	-	-	-	1.91	27.1
CW_750_D	528	0.287	0.205	0.082	1.93	26.1
CAS_700_K_1:2	1777	0.722	0.690	0.032	2.08	14.2
CAS_750_K_1:1	1346	0.655	0.518	0.137	2.02	21.3
CAS_750_K_1:2	2440	1.100	1.072	0.028	2.12	13.9
CAS_750_K_1:3	2815	1.224	1.216	0.008	2.36	10.9
CAS_800_K_1:2	2356	1.029	1.017	0.012	2.44	13.0

^a Calculated at $p/p^0 = 0.99$; ^b calculated with the DR method; ^c $V_{meso} = V_{total} - V_{micro}$; ^d expressed as $(mass_{monolith}/mass_{whey}) \times 100$.

The effect of the monolith/CH ratio on the KOH activation was as expected. For a given temperature (750 °C), increasing the KOH content increases the total pore volume of the monoliths from 0.655 to 1.224 cm³/g. The microporosity is enhanced as one moves from CAS_750_K_1:1 to CAS_750_K_1:3, whereas the mesopore volume diminishes quickly (Table 2). A close look to the PSD of these materials (Figure 7b) shows how the initially wide mesopores (>5 nm) present in CAS_750_K_1:1 disappear as the relative CH ratio increases (i.e., samples CAS_X_K_1:2 and CAS_X_K_1:3, with X being 750 or 800), with narrow mesopores with an average diameter of around 2.8 nm evolving in those samples. The origin of the wide mesopores in sample CAS_750_K_1:1 should be related to the precursor porosity [45]. Since the carbonised whey CW_750 shows no significant N₂ adsorption at cryogenic temperatures, the origin of the wide mesoporosity of CAS_750_K_1:1 should be related to the washing carried out after the KOH activation to remove byproducts (mainly carbonates). To check this possibility, a CW_750 monolith was thoroughly washed with HCl and water following the same methodology used for the KOH-activated monoliths. The N₂ adsorption isotherm and textural parameters of the CW_750_D monolith are also included in Figure 7 and Table 2. It is clear that (i) a simple demineralisation process increases significantly the porosity (as determined by the N₂ adsorption) of the whey carbon monoliths, with mineral species in the CWs blocking the entrance to pores; and (ii) mesopores are a significant part of CW_750_D porosity, with a PSD resembling that of CAS_750_K_1:1 (see inset in Figure 7b).

As for the effect of the activation temperature [45], for a given monolith/CH ratio (1:2), results fulfilled the expectances only partially. Increasing the heat treatment temperature from 700 °C to 750 °C leads to an important increment in the porosity of the monoliths (Figure 7 and Table 2). However, a further rise to 800 °C has little effect in either the specific surface area or pore volumes.

The effectiveness of the KOH activation when compared to thermal activation is clearly demonstrated with materials reaching S_{BET} values up to 2815 m²/g and a $V_{\text{total}} = 1.224$ cm³/g for the maximum chemical agent ratio tested (1:3). Moreover, the yields of the activated monoliths per specific surface area are much higher in the case of the KOH-activated samples (Tables 1 and 2). In spite of this latter observation, the harshness of the alkali activation caused at least the presence of cracks that were evident after ocular inspection of the monoliths (Figure 5). In some cases, CAS_750_K_1:3 and CAS_800_K_1:2, the breakdown of the monoliths in several pieces occurred, thus limiting strongly the feasibility of this type of activation to obtain customised 3D microporous carbons.

3.3.2. H₃PO₄ Activation

As in the case of the KOH activation, we explored the effect of the CH relative proportion and the activation temperature variables on the outcome. Figure 8 shows the N₂ adsorption isotherms (−196 °C) of the H₃PO₄ activated samples, with Table 3 collecting the principal textural parameters calculated. All phosphoric activated monoliths isotherms are a combination of Type I and Type IV for microporous materials with a certain amount of mesopores and hysteresis loop type H4 for slit-shaped pores. The isotherms have open “knees” in the micropore relative pressure range, which indicates a lower contribution of microporosity to the total pore volume. This contrasts with the KOH-activated samples showing isotherms with very close “knees”. Thus, comparing the samples with similar V_{total} values (i.e., CAS_750_K_1:1 and CAS_800_P_1:2, Tables 2 and 3, respectively), the KOH-activated samples exhibit significantly higher S_{BET} and V_{micro} than the H₃PO₄-activated samples. As a consequence, the contribution of mesoporosity to the V_{total} is the highest for this type of activation. The N₂ PSDs of all the phosphoric-activated samples (Figure 8b) point out that a relatively sharp, unimodal distribution in the mesoporosity range is common to all monoliths, with maxima located at ca. 3 nm (i.e., narrow mesopores).

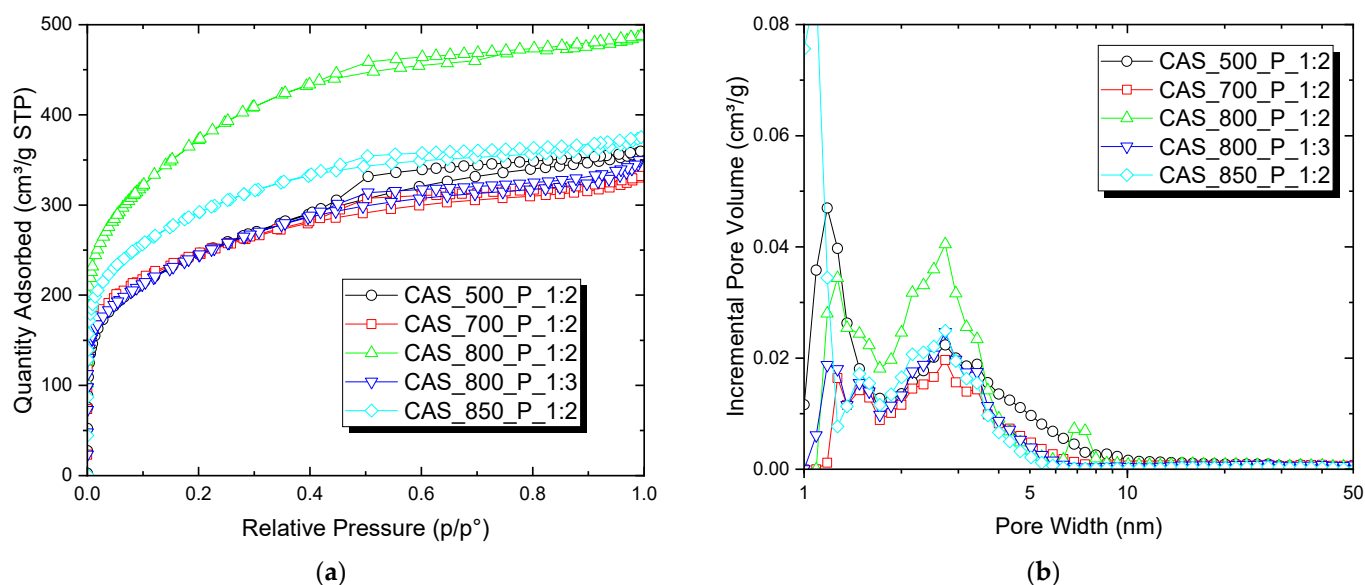


Figure 8. (a) N₂ adsorption isotherms (−196 °C); and (b) DFT pore size distributions of the chemically (H₃PO₄) activated monoliths derived from whey.

Table 3. Selected textural parameters and yields of the chemically (H₃PO₄) activated carbon monoliths.

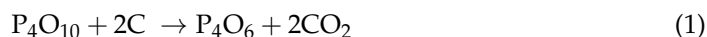
Sample	S _{BET} (m ² /g)	V _{total} ^a (cm ³ /g)	V _{micro} ^b (cm ³ /g)	V _{meso} ^c (cm ³ /g)	ρ _{He} (g/cm ³)	Yield ^d (%)
CAS_500_P_1:2	893	0.554	0.329	0.225	1.64	33.7
CAS_700_P_1:2	891	0.511	0.303	0.208	1.83	31.8
CAS_800_P_1:2	1354	0.751	0.438	0.313	2.00	23.7
CAS_800_P_1:3	886	0.539	0.297	0.242	1.93	26.4
CAS_850_P_1:2	1062	0.578	0.372	0.206	1.93	22.1

^a Calculated at $p/p^0 = 0.99$; ^b calculated with the DR method; ^c $V_{meso} = V_{total} - V_{micro}$; ^d expressed as $(mass_{monolith}/mass_{whey}) \times 100$.

The possibility of using different thermally stabilised whey:H₃PO₄ ratios was very limited and restricted in practice to a 1:2 ratio. The thermally stabilised whey: H₃PO₄ ratios of 1:1 produced little to no pore development, whereas the use of higher ratios (1:3) led to the overactivation of the monoliths. This latter observation is exemplified with the samples CAS_800_P_1:2 and CAS_800_P_1:3 in Figure 8 and Table 3. Increasing the relative proportion of the CH brings about a monolith with lower textural parameters. It has been reported that, when using high phosphoric acid impregnation ratios at relatively high (800 °C) activation temperatures, the progressive formation of polyphosphates and C-O-P bonds could block the pore entrances and lead to some loss of porosity, since these phosphate-like species are not easily removed in the washing process [46]. This would also justify the higher yield of CAS_800_P_1:3 when compared to that of CAS_800_P_1:2 (Table 3).

Regarding the effect of the activation temperature, although the activation with H₃PO₄ works better at lower temperatures for lignocellulosic precursors [47,48], in this case, results show that higher temperatures (800 °C) are necessary to obtain an optimal porous development (Figure 8), with a maximum S_{BET} for sample CAS_800_P_1:2 of 1354 m²/g (Table 3). This could be attributed to the different mechanisms involved in the activation with phosphoric acid. In the activation at low temperatures (500 °C) of the thermally stabilised (250 °C, in this case) whey monoliths, the porosity is mainly produced by the elimination of volatile matter (Figure 3) catalysed by the dehydration of the phosphoric acid, which promotes bond cleavage reactions and crosslinking formation via processes such as cyclisation and condensation [47,48]. Activation at higher temperatures (>500 °C) provokes, in some cases, the collapse of the porous network. However, when the activation temperature rises to 700 °C, the structure of the whey carbon is strong enough to maintain the microporosity developed at earlier stages (hence the similar pore development of samples CAS_500_P_1:2 and CAS_700_P_1:2), with a slight densification taking place as shown by the significant increase in the real density (ρ_{He}) of the CAS_700_P_1:2 sample.

As just mentioned, the most important pore development occurs at 800 °C, sample CAS_800_P_1:2. The activation mechanism of phosphoric acid at such relatively high temperatures is different to that already discussed. At this temperature, H₃PO₄ dehydrates and transforms into P₄O₁₀ [40]. This latter moiety behaves in the absence of water as an oxidant reacting with the carbon matrix as follows [48]:



The formation of volatile phosphorous-containing compounds as a result of the present phosphate reduction and the introduction of phosphorus species into the carbon structure through C-O-P bonds led to the formation of new pores and the widening of the existent pores. At the same time, the reaction between the evolved CO₂ and the carbon skeleton results in an additional increase in porosity. Depending on the precursors, some authors report the presence of PH₄ and elemental P₄ as products of the high-temperature phosphoric

activation of carbons [48–50]. These phosphorous species are easily removed in the washing process thus leaving pores available. Finally, further rising the activation temperature up to 850 °C (sample CAS_850_P_1:2) backtracks in terms of the pore development, thus suggesting that some of the micro- and narrow mesoporosity start to collapse.

Although the porous development of the H₃PO₄-activated samples is poorer compared with the KOH-activated samples, the yields are considerably higher, higher even than the thermally activated ones. This would make this activation very interesting, although we could not obtain samples free of cracks (Figure 5) under the activation conditions tested.

3.4. Further Characterisation of Selected Samples

Five monolithic samples combining high specific surface area and (in principle) good mechanical integrity, namely CW_850, CW_750_D, TAW_850_1.5, CAS_750_K_1:2, and CAS_800_P_1:2 were further characterised using different techniques.

To complete the characterisation of the porosity of the monoliths, the selected samples were analysed by Hg intrusion. Figure 9 shows the PSD obtained by Hg intrusion with the corresponding main textural parameters collected in Table 4. All monoliths show an important macroporous development with the maxima of the Hg PSD centred at ca. 27 µm, except in the case of TAW_850_1.5, for which the Hg PSD is slightly shifted to smaller pore sizes values (Table 4). The percentage of porosity of the activated samples is >70%, with sample CAS_750_K_1:2 showing an outstanding 82% porosity value. The widening of the PSD of CAS_750_K_1:2 in the lower pore sizes region is also evident. This might suggest that the intrusion of Hg is damaging the sample. The same observation also stands when analysing the PSD of the monoliths in the mesoporous region. The relatively high V_{meso} (as determined with Hg intrusion) of CAS_750_K_1:2 was totally unexpected in the light of its N₂ adsorption isotherm (Figure 7). Actually, the only monoliths that show significant V_{meso} values in the Hg intrusion characterisation are the activated ones (Table 4), thus pointing out that the monoliths might not be bearing such massive pressures.

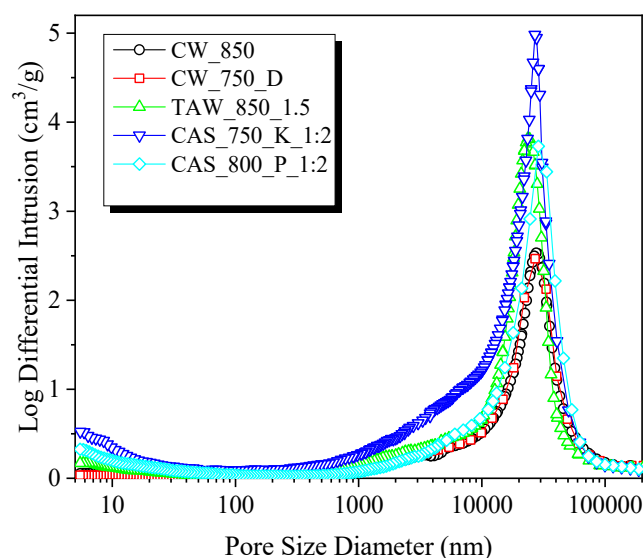


Figure 9. Pore size distributions (PSD) of selected monoliths as measured by Hg intrusion.

The elemental analyses, moisture and ash contents of the selected monoliths are collected in Table 5. Both CW_850 and TAW_850_1.5 samples have the highest ash contents. The demineralisation of the carbonised samples and the cleaning of the by-products after the chemically activated monoliths remove most of the ashes leaves only <4% leftover. Those two samples also contain the highest moisture values and oxygen contents, and the lowest carbon contents, all of which being related to their high ash content. It is also remarkable the high nitrogen content that remains in the carbon structure of the activated monoliths ($\geq 3\%$), regardless of the activation procedure. Specifically, chemical activation

had little effect on the final nitrogen content of the monoliths. This is especially relevant for a broad spectrum of electrochemical applications with special interest in natural and induced nitrogen carbon materials [51–53]. This is very interesting since all this nitrogen content is naturally present in the whey powders, i.e., there is no need for an extra nitrogen source for N-doping. Furthermore, the N content of these materials surpasses even those reported for N-doped mesoporous carbons derived from tannins, as well as the microporous carbons derived from various natural biowaste fibres that have been modified with different nitrogen source species, such as urea or melamine [54,55]. Finally, monolithic materials with very different surface chemistry in terms of acidity/basicity, as determined by the pH_{PZC} , were obtained.

Table 4. Textural parameters of selected monoliths obtained from Hg intrusion data.

Sample	V_{Hg}^a (cm^3/g)	V_{macro}^b (cm^3/g)	V_{meso}^c (cm^3/g)	d_{max}^d (μm)	ρ_{Hg} (g/cm^3)	s^e (wt.%)
CW_850	1.435	1.435	-	27.3	0.85	57
CW_750_D	1.493	1.469	-	27.1	0.85	59
TA_850_1.5	1.947	1.854	0.094	23.7	0.62	70
CAS_750_K_1:2	2.378	2.134	0.245	27.0	0.38	82
CAS_800_P_1:2	2.038	1.884	0.145	28.8	0.57	72

^a Volume of intruded Hg; ^b volume of Hg intruded in pores with sizes > 50 nm; ^c $V_{\text{meso}} = V_{\text{Hg}} - V_{\text{macro}}$; ^d pore size of the PSD maximum; ^e open porosity, $s = [1 - (\rho_{\text{Hg}}/\rho_{\text{He}})] \times 100$.

Table 5. Elemental analysis, moisture and ash contents, and pH_{PZC} of selected monoliths.

Sample	C ^a (wt.%)	H ^a (wt.%)	N ^a (wt.%)	S ^a (wt.%)	O ^a (wt.%)	Moisture ^b (wt.%)	Ash ^b (wt.%)	pH_{PZC}
CW_850	68.0	1.2	2.3	0.2	13.4	12.2	6.1	11.1
CW_750_D	88.5	0.8	3.0	0.2	6.6	6.2	2.7	5.2
TA_850_1.5	64.5	0.8	3.0	0.2	14.0	13.7	18.1	11.3
CAS_750_K_1:2	88.3	0.5	3.2	0.2	6.7	9.6	3.0	4.8
CAS_800_P_1:2	82.3	1.2	3.1	0.0	11.4	7.8	3.8	2.4

^a Elemental analysis, dry basis; ^b proximate analysis, wet basis.

3.5. Mechanical Properties of Selected Monoliths

Mechanical properties of the selected samples were evaluated by compressive tests. Figure 10a shows typical strain/stress curves of the tested materials. Two of the monoliths, the chemically activated CAS_750_K_1:2 and CAS_800_P_1:2, could not bear any load during the compressive test, i.e., the structures shattered as soon as the load started to build up. The crevices on the surface of the chemically activated monoliths acted as fracture initiators that propagated quickly and destroyed the structures. Conversely, the compressive test curves of the CW_850 and CW_850_D monoliths increased monotonically within the elastic linear zone of the curve until the experiment reached the point of failure. This behaviour is characteristic of ceramic materials presenting brittle failure. Finally, a clear difference is observed in the stress/strain curve of the thermally activated monolith TA_850_1.2. In this case, the curve progresses with some breaks or jumps, which could indicate small fractures or imperfections in the monolith. After these discontinuities in the curve, the stress recovers almost immediately and the monolith is capable of bearing loads up to higher strain values, when compared to CW_850 and CW_850_D. The imperfections/fractures change the monolith failure mode to non-brittle, and if they exacerbate, as in the case of the chemically activated monoliths and the thermally activated monoliths under more severe conditions, thus leading to surface crevices (Figure 5), the monolith cannot bear a substantial load.

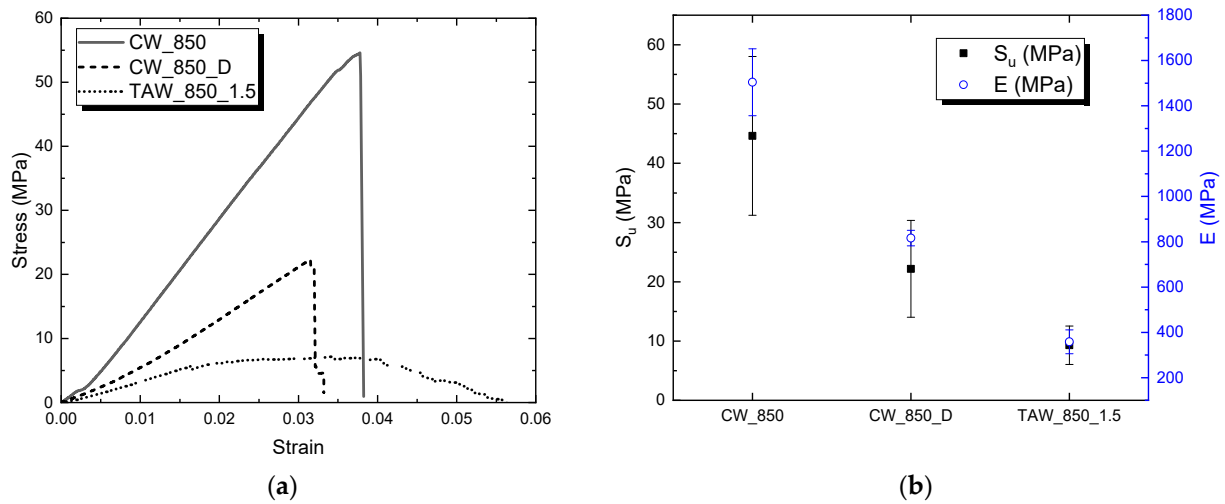


Figure 10. (a) Examples of stress/strain curves; and (b) strength (S_u) and modulus (E) of selected carbon monoliths.

Figure 10b shows the average values (and standard deviations) of the compressive strength (S_u) and modulus (E) of CW_850, CW_750_D, and TAW_850_1.5. The monolith elastic modulus goes down with porosity, from 1.5 GPa to 350 MPa for CW_850_D and TAW_850_1.5, respectively. This latter value is, however, much higher than the elastic modulus reported for hierarchical carbon monoliths made from glucose (1 MPa) [56]. In the case of CW_850, the S_u value is over 40 MPa, which is superior to other porous carbons and even ceramic materials with similar porosities. As the porosity of the monoliths increases, the compressive strength decreases (Figure 11). In this way, CW_850_D presents values around 20 MPa, while for TAW_850_1.5 the value of S_u drops to ca. 10 MPa. However, all these values are still very remarkable and considerably higher than those of other activated carbons found in the literature (Figure 11, red symbols) [19,20,57–62], specifically those made from coal (red triangles) [19], or those that are resin-based [57]. The red star of Figure 11 corresponds to a ceramic (cordierite)/carbon monolith [62].

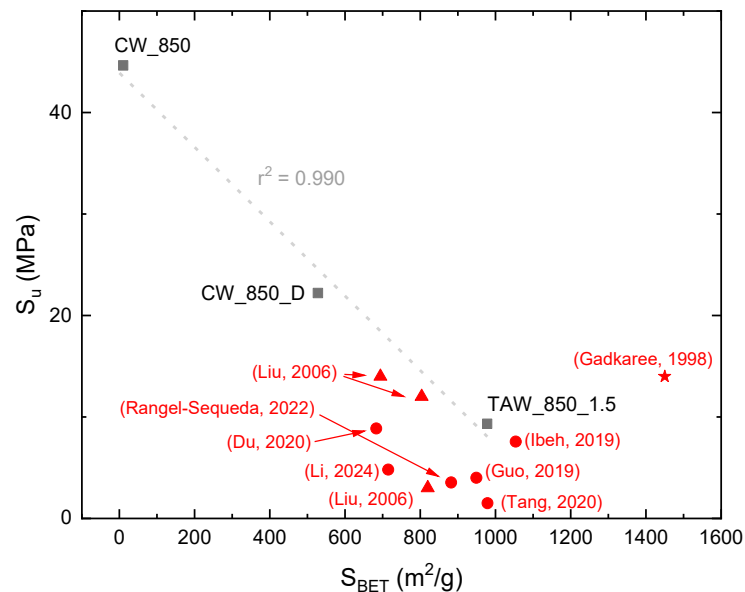


Figure 11. Correlation between S_u and S_{BET} of the selected carbon monoliths made from whey (black squares). The red symbols are results of other activated carbon monoliths found in the literature: (Liu, 2006) [19]; (Rangel-Sequeda, 2022) [20]; (Du, 2020) [57]; (Li, 2024) [58]; (Ibeh, 2019) [59]; (Guo, 2019) [60]; (Tang, 2020) [61]; (Gadkaree, 1998) [62].

4. Conclusions

A simple and novel method is presented for synthesising highly porous 3D carbon structures. These carbon monoliths can be easily moulded to specific shapes and machined for specific applications. They are easily produced by pseudo-sintering dehydrated whey powders at high temperatures, which promote self-reaction between the precursor components (specifically lactose and whey proteins) with no need for external binders, overpressure, or templates. A mechanically strong porous carbon 3D structure with a hierarchical macro/meso/microporosity can be obtained simply by demineralising the whey carbon monoliths. The monolithic shape is preserved upon thermal activation with CO₂ and chemical activation with KOH or H₃PO₄, resulting in high porosities and S_{BET} up to 2400 m²/g, although chemical activation affects critically the mechanical properties of the 3D structures. The final carbonised, demineralised, and thermally activated monoliths have exceptional mechanical properties and an interconnected porous structure. In addition, they have a notable natural nitrogen content of up to 3 wt.%.

The possibility of using whey as a precursor of activated carbon monoliths constitutes a modest alternative for whey valorisation, in addition to lessening their dependence on fossil-fuel derived precursors. These two outcomes are significant in a circular economy model of materials/goods production and consumption.

Author Contributions: Conceptualization, L.A.R.-M., J.A.M. and M.A.M.-M.; methodology, all authors; investigation, R.L.-U. and L.A.R.-M.; writing—original draft preparation, L.A.R.-M.; writing—review and editing, all authors; funding acquisition, J.A.M. and M.A.M.-M. All authors have read and agreed to the published version of the manuscript.

Funding: This research was funded by the Spanish Ministerio de Ciencia e Innovación (MCIN/AEI/10.13039/501100011033) (Project PID2020-115334GB-I00) and Principado de Asturias (FICYT)—European Union (FEDER) (Project PCTI-Asturias IDI/2021/000015). L.A.R.-M. thanks CONACYT, Mexico, for a postdoctoral grant (CVU No. 330625, 2022).

Data Availability Statement: The data presented in this study are available on request from the corresponding author.

Acknowledgments: J. Angel Menéndez and Miguel Montes are members of the CSIC Interdisciplinary Thematic Platform (PTI+) for Sustainable Plastics towards a Circular Economy (PTI-SusPlast+).

Conflicts of Interest: The authors declare no conflict of interest. The funders had no role in the design of the study; in the collection, analyses, or interpretation of the data; in the writing of the manuscript; or in the decision to publish the results.

References

1. Lan, G.; Yang, J.; Ye, R.-P.; Boyjoo, Y.; Liang, J.; Liu, X.; Li, Y.; Liu, J.; Qian, K. Sustainable carbon materials toward emerging applications. *Small Methods* **2021**, *5*, 2001250. [[CrossRef](#)] [[PubMed](#)]
2. Yap, Y.W.; Mahmed, N.; Norizan, M.N.; Abd Rahim, S.Z.; Ahmad Salimi, M.N.; Abdul Razak, K.; Mohamad, I.S.; Abdullah, M.M.A.-B.; Mohamad Yunus, M.Y. Recent advances in synthesis of graphite from agricultural bio-waste material: A review. *Materials* **2023**, *16*, 3601. [[CrossRef](#)] [[PubMed](#)]
3. Wang, Y.; Zhang, M.; Shen, X.; Wang, H.; Wang, H.; Xia, K.; Yin, Z.; Zhang, Y. Biomass-derived carbon materials: Controllable preparation and versatile applications. *Small* **2021**, *17*, 2008079. [[CrossRef](#)] [[PubMed](#)]
4. Chakraborty, R.; Vilya, K.; Pradhan, M.; Nayak, A.K. Recent advancement of biomass-derived porous carbon based materials for energy and environmental remediation applications. *J. Mater. Chem. A* **2022**, *10*, 6965–7005. [[CrossRef](#)]
5. Chen, Q.; Tan, X.; Liu, Y.; Liu, S.; Li, M.; Gu, Y.; Zhang, P.; Ye, S.; Yang, Z.; Yang, Y. Biomass-derived porous graphitic carbon materials for energy and environmental applications. *J. Mater. Chem. A* **2020**, *8*, 5773–5811. [[CrossRef](#)]
6. Sun, L.; Gong, Y.; Li, D.; Pan, C. Biomass-derived porous carbon materials: Synthesis, designing, and applications for supercapacitors. *Green Chem.* **2022**, *24*, 3864–3894. [[CrossRef](#)]
7. Crittenden, B.; Patton, A.; Jouin, C.; Perera, S.; Tennison, S.; Botas Echevarria, J.A. Carbon monoliths: A comparison with granular materials. *Adsorption* **2005**, *11*, 537–541. [[CrossRef](#)]
8. Vilaplana-Ortego, E.; Alcañiz-Monge, J.; Cazorla-Amorós, D.; Linares-Solano, A. Activated carbon fibre monoliths. *Fuel Process. Technol.* **2002**, *77–78*, 445–451. [[CrossRef](#)]
9. Moreno-Castilla, C.; Pérez-Cárdenas, A.F. Carbon-based honeycomb monoliths for environmental gas-phase applications. *Materials* **2010**, *3*, 1203–1227. [[CrossRef](#)]

10. Yu, F.D.; Luo, L.A.; Grevillot, G. Adsorption isotherms of VOCs onto an activated carbon monolith: Experimental measurement and correlation with different models. *J. Chem. Eng. Data* **2002**, *47*, 467–473. [[CrossRef](#)]
11. Yates, M.; Martín-Luengo, M.A.; Vega Argomaniz, L.; Nogales Velasco, S. Design of activated carbon–clay composites for effluent decontamination. *Microporous Mesoporous Mater.* **2012**, *154*, 87–92. [[CrossRef](#)]
12. McIntosh, S.L.; Herkes, F.E.; Keller, J.H. Activated carbon monolith catalysts (ACMC): A new and novel catalyst system. *Top. Catal.* **2010**, *53*, 1091–1095. [[CrossRef](#)]
13. Gatica, J.M.; Gómez, D.M.; Vidal, H. Monolithic honeycomb design applied to carbon materials for catalytic methane decomposition. *Appl. Catal. A* **2013**, *458*, 21–27. [[CrossRef](#)]
14. Marco-Lozar, J.P.; Kunowsky, M.; Suárez-García, F.; Carruthers, J.D.; Linares-Solano, A. Activated carbon monoliths for gas storage at room temperature. *Energy Environ. Sci.* **2012**, *5*, 9833–9842. [[CrossRef](#)]
15. Reljic, S.; Cuadrado-Collados, C.; Farrando-Perez, J.; Jardim, E.O.; Martinez-Escandell, M.; Silvestre-Albero, J. Carbon-based monoliths with improved thermal and mechanical properties for methane storage. *Fuel* **2022**, *324*, 124753. [[CrossRef](#)]
16. Romero-Anaya, A.J.; Kunowsky, M.; Rufete-Beneite, M.; Lillo-Ródenas, M.Á.; Linares-Solano, A. Novel monoliths prepared from sucrose avoiding binder and thermal treatment. *Microporous Mesoporous Mater.* **2019**, *284*, 78–81. [[CrossRef](#)]
17. Liu, L.; Liu, Z.; Huang, Z.; Liu, Z.; Liu, P. Preparation of activated carbon honeycomb monolith directly from coal. *Carbon* **2006**, *44*, 1598–1601. [[CrossRef](#)]
18. Jordá-Beneyto, M.; Lozano-Castelló, D.; Suárez-García, F.; Cazorla-Amorós, D.; Linares-Solano, A. Advanced activated carbon monoliths and activated carbons for hydrogen storage. *Microporous Mesoporous Mater.* **2008**, *112*, 235–242. [[CrossRef](#)]
19. Liu, L.; Liu, Z.; Yang, J.; Huang, Z.; Liu, Z. Effect of preparation conditions on the properties of a coal-derived activated carbon honeycomb monolith. *Carbon* **2007**, *45*, 2836–2842. [[CrossRef](#)]
20. Rangel-Sequeda, J.F.; Loredó-Cancino, M.; Águeda Maté, V.I.; De Haro-Del Rio, D.A.; Dávila-Guzmán, N.E. 3D printing of powdered activated carbon monoliths: Effect of structuring on physicochemical and mechanical properties and its influence on the adsorption performance. *Mat. Today Commun.* **2022**, *33*, 104758. [[CrossRef](#)]
21. Lozano-Castelló, D.; Cazorla-Amorós, D.; Linares-Solano, A.; Quinn, D.F. Activated carbon monoliths for methane storage: Influence of binder. *Carbon* **2002**, *40*, 2817–2825. [[CrossRef](#)]
22. Ramos-Fernández, J.M.; Martínez-Escandell, M.; Rodríguez-Reinoso, F. Production of binderless activated carbon monoliths by KOH activation of carbon mesophase materials. *Carbon* **2008**, *46*, 365–389. [[CrossRef](#)]
23. Nakagawa, Y.; Molina-Sabio, M.; Rodríguez-Reinoso, F. Modification of the porous structure along the preparation of activated carbon monoliths with H₃PO₄ and ZnCl₂. *Microporous Mesoporous Mater.* **2007**, *103*, 29–34. [[CrossRef](#)]
24. Vargas, D.P.; Giraldo, L.; Moreno-Piraján, J.C. CO₂ adsorption on activated carbon honeycomb-monoliths: A comparison of Langmuir and Tóth models. *Int. J. Mol. Sci.* **2012**, *13*, 8388–8397. [[CrossRef](#)] [[PubMed](#)]
25. Ibeh, P.O.; García-Mateos, F.J.; Ruiz-Rosas, R.; Rosas, J.M.; Rodríguez-Mirasol, J.; Cordero, T. Acid mesoporous carbon monoliths from lignocellulosic biomass waste for methanol dehydration. *Materials* **2019**, *12*, 2394. [[CrossRef](#)]
26. Budarin, V.L.; Shuttleworth, P.S.; White, R.J.; Clark, J.H. From polysaccharides to starbons[®]. *RSC Green Chem.* **2015**, *32*, 53–81. [[CrossRef](#)]
27. Castro-Gutiérrez, J.; Sanchez-Sanchez, A.; Ghanbaja, J.; Díez, N.; Sevilla, M.; Celzard, A.; Fierro, V. Synthesis of perfectly ordered mesoporous carbons by water-assisted mechanochemical self-assembly of tannin. *Green Chem.* **2018**, *20*, 5123–5132. [[CrossRef](#)]
28. Dodson, J.R.; Budarin, V.L.; Hunt, J.; Shuttleworth, P.S.; Clark, J.H. Shaped mesoporous materials from fresh macroalgae. *J. Mater. Chem. A* **2013**, *1*, 5203–5307. [[CrossRef](#)]
29. Titirici, M.-M.; Antonietti, M. Chemistry and materials options of sustainable carbon materials made by hydrothermal carbonization. *Chem. Soc. Rev.* **2010**, *39*, 103–116. [[CrossRef](#)]
30. Antonietti, M.; Fechner, N.; Feller, T.-P. Carbon aerogels and monoliths: Control of porosity and nanoarchitecture via sol-gel routes. *Chem. Mater.* **2007**, *19*, 4205–4212. [[CrossRef](#)]
31. Llamas-Unzueta, R.; Menéndez, J.A.; Ramírez-Montoya, L.A.; Viña, J.; Argüelles, A.; Montes-Morán, M.A. 3-D structured porous carbons with virtually any shape from whey powders. *Carbon* **2021**, *175*, 403–412. [[CrossRef](#)]
32. Prazeres, A.; Carvalho, M.d.F.; Rivas, J. Cheese whey management: A review. *J. Environ. Manag.* **2012**, *110*, 48–68. [[CrossRef](#)]
33. González-Weller, D.; Paz-Montelongo, S.; Bethencourt-Barbuzano, E.; Niebla-Canelo, D.; Alejandro-Vega, S.; Gutiérrez, A.J.; Hardisson, A.; Carrascosa, C.; Rubio, C. Proteins and minerals in whey protein supplements. *Foods* **2023**, *12*, 2238. [[CrossRef](#)]
34. Zadow, J. *Whey and Lactose Processing*; Elsevier Science Publishers Ltd.: Essex, UK, 1992.
35. Barba, F.J. An integrated approach for the valorization of cheese whey. *Foods* **2021**, *10*, 564. [[CrossRef](#)] [[PubMed](#)]
36. Llamas-Unzueta, R.; Suárez, M.; Fernández, A.; Díaz, R.; Montes-Morán, M.A.; Menéndez, J.A. Whey-derived porous carbon scaffolds for bone tissue engineering. *Biomedicines* **2021**, *9*, 1091. [[CrossRef](#)] [[PubMed](#)]
37. Tan, S.; Chen, X.; Zhai, S.; Ebrahimi, A.; Langrish, T.; Chen, Y. Spray drying assisted synthesis of porous carbons from whey powders for capacitive energy storage. *Energy* **2018**, *147*, 308–316. [[CrossRef](#)]
38. Pokrzywinski, J.; Keum, J.K.; Ruther, R.E.; Self, E.C.; Chi, M.; Meyer, H.; Littrell, K.C.; Aulakh, D.; Marble, S.; Ding, J.; et al. Unrivaled combination of surface area and pore volume in micelle-templated carbon for supercapacitor energy storage. *J. Mater. Chem. A* **2017**, *5*, 13511–13525. [[CrossRef](#)]
39. Menéndez, J.A.; Illán-Gómez, M.; León, C.Y.; Radovic, L. On the difference between the isoelectric point and the point of zero charge of carbons. *Carbon* **1995**, *33*, 1655–1657. [[CrossRef](#)]

40. Llamas-Unzueta, R.; Menéndez, J.A.; Suárez, M.; Fernández, A.; Montes-Morán, M.A. From whey robocasting to 3D porous carbons. *Add. Manufact.* **2022**, *59*, 103083. [[CrossRef](#)]
41. Zhang, Q.; Chen, M.; Emilia Coldea, T.; Yang, H.; Zhao, H. Structure, chemical stability and antioxidant activity of melanoidins extracted from dark beer by acetone precipitation and macroporous resin adsorption. *Food Res. Int.* **2023**, *164*, 112045. [[CrossRef](#)] [[PubMed](#)]
42. De la Rosa Arranz, J.M.; González-Vila, F.J.; López-Capel, E.; Manning, D.A.C.; Knicker, H.; González-Pérez, J.A. Structural properties of non-combustion-derived refractory organic matter which interfere with BC quantification. *J. Anal. Appl. Pyrol.* **2009**, *85*, 399–407. [[CrossRef](#)]
43. Llamas-Unzueta, R.; Montes-Morán, M.A.; Ramírez-Montoya, L.A.; Concheso, A.; Menéndez, J.A. Whey as a sustainable binder for the production of extruded activated carbon. *J. Environ. Chem. Eng.* **2022**, *10*, 107590. [[CrossRef](#)]
44. Lopez, M.; Labady, M.; Laine, J. Preparation of activated carbon from wood monolith. *Carbon* **1996**, *34*, 825–827. [[CrossRef](#)]
45. Linares-Solano, A.; Lozano-Castelló, D.; Lillo-Ródenas, M.A.; Cazorla-Amorós, D. Carbon activation by alkaline hydroxides preparation and reactions, porosity and performance. *Chem. Phys. Carbon* **2008**, *30*, 2–64–62. [[CrossRef](#)]
46. Liou, T.-H.; Wu, S.-J. Characteristics of microporous/mesoporous carbons prepared from rice husk under base- and acid-treated conditions. *J. Hazard. Mater.* **2009**, *171*, 693–703. [[CrossRef](#)]
47. Jagtoyen, M.; Derbyshire, F. Activated carbons from yellow poplar and white oak by H₃PO₄ activation. *Carbon* **1998**, *36*, 1085–1097. [[CrossRef](#)]
48. Li, Y.; Zhang, X.; Yang, R.; Li, G.; Hu, C. The role of H₃PO₄ in the preparation of activated carbon from NaOH-treated rice husk residue. *RSC Adv.* **2015**, *5*, 32626–32636. [[CrossRef](#)]
49. Myglovets, M.; Poddubnaya, O.I.; Sevastyanova, O.; Lindström, M.E.; Gawdzik, B.; Sobiesiak, M.; Tsyba, M.M.; Sapsay, V.I.; Klymchuk, D.O.; Puziy, A.M. Preparation of carbon adsorbents from lignosulfonate by phosphoric acid activation for the adsorption of metal ions. *Carbon* **2014**, *80*, 771–783. [[CrossRef](#)]
50. Puziy, A.M.; Poddubnaya, O.I.; Socha, R.P.; Gurgul, J.; Wisniewski, M. XPS and NMR studies of phosphoric acid activated carbons. *Carbon* **2008**, *46*, 2113–2123. [[CrossRef](#)]
51. Bejjanki, D.; Banothu, P.; Kumar, V.B.; Kumar, P.S. Biomass-derived N-doped activated carbon from eucalyptus leaves as an efficient supercapacitor electrode material. *C* **2023**, *9*, 24. [[CrossRef](#)]
52. Liao, Y.; Shang, Z.; Ju, G.; Wang, D.; Yang, Q.; Wang, Y.; Yuan, S. Biomass derived N-doped porous carbon made from reed straw for an enhanced supercapacitor. *Molecules* **2023**, *28*, 4633. [[CrossRef](#)]
53. Inagaki, M.; Toyoda, M.; Soneda, Y.; Morishita, T. Nitrogen-doped carbon materials. *Carbon* **2018**, *132*, 104–140. [[CrossRef](#)]
54. Liu, F.; Gao, Y.; Zhang, C.; Huang, H.; Yan, C.; Chu, X.; Xu, Z.; Wang, Z.; Zhang, H.; Xiao, X.; et al. Highly microporous carbon with nitrogen-doping derived from natural biowaste for high-performance flexible solid-state supercapacitor. *J. Coll. Interf. Sci.* **2019**, *548*, 322–332. [[CrossRef](#)]
55. Zhao, J.; Shan, W.; Zhang, P.; Dai, S. Solvent-free and mechanochemical synthesis of N-doped mesoporous carbon from tannin and related gas sorption property. *Chem. Eng. J.* **2020**, *381*, 122579. [[CrossRef](#)]
56. Estevez, L.; Dua, R.; Bhandari, N.; Ramanujapuram, A.; Wang, P.; Giannelis, E.P. A facile approach for the synthesis of monolithic hierarchical porous carbons-high performance materials for amine based CO₂ capture and supercapacitor electrode. *Energy Environ. Sci.* **2013**, *6*, 1785–1790. [[CrossRef](#)]
57. Du, J.; Li, W.C.; Ren, Z.X.; Guo, L.P.; Lu, A.H. Synthesis of mechanically robust porous carbon monoliths for CO₂ adsorption and separation. *J. Energy Chem.* **2020**, *42*, 56–61. [[CrossRef](#)]
58. Li, D.; Tian, Y.; Qiao, Y.; Wen, L. Conversion of powdered active carbon into monoliths without reducing specific surface area using H₃PO₄-impregnated waste sawdust. *Mater. Lett.* **2024**, *125*, 175–178. [[CrossRef](#)]
59. Ibeh, P.O.; García-Mateos, F.J.; Rosas, J.M.; Rodríguez-Mirasol, J.; Cordero, T. Activated carbon monoliths from lignocellulosic biomass waste for electrochemical applications. *J. Taiwan Inst. Chem. Eng.* **2019**, *97*, 480–488. [[CrossRef](#)]
60. Guo, L.P.; Li, W.C.; Qiu, B.; Ren, Z.X.; Dua, J.; Lu, A.H. Interfacial assembled preparation of porous carbon composites for selective CO₂ capture at elevated temperatures. *J. Mater. Chem. A* **2019**, *7*, 5402–5408. [[CrossRef](#)]
61. Tang, S.H.; Zaini, M.A.A. Development of activated carbon pellets using a facile low-cost binder for effective malachite green dye removal. *J. Clean. Prod.* **2020**, *253*, 119970. [[CrossRef](#)]
62. Gadkaree, K.P. Carbon honeycomb structures for adsorption applications. *Carbon* **1998**, *36*, 981–989. [[CrossRef](#)]

Disclaimer/Publisher's Note: The statements, opinions and data contained in all publications are solely those of the individual author(s) and contributor(s) and not of MDPI and/or the editor(s). MDPI and/or the editor(s) disclaim responsibility for any injury to people or property resulting from any ideas, methods, instructions or products referred to in the content.